IJETIR

ISSN (Online) 2583-0554

International Journal of Emerging Technologies and Innovative Research (IJETIR)

Volume 3, Issue 3, March 2023

Impact Factor: 5.731

Fabrication, Screen Printing and X-ray Diffraction Pattern of ZnO Thick Films

Sudhakar Vitthalrao Maske
Department of Physics
I.C.S. College of Arts, Commerce and Science Khed, Ratnagiri, India
Corresponding author: sudhakarmaske@gmail.com

Abstract: *Zinc oxide (ZnO) thick films were fabricated via screen printing using nanopowders synthesized by co-precipitation. A 0.5 M $ZnCl_2$ solution underwent dropwise addition of 1.0 M NaOH under vigorous stirring (800 rpm), forming a zinc hydroxide colloid. The precipitate was vacuum-filtered (0.2 µm membrane), washed, dried (25°C, 24 h), and calcined at 400°C (5°C/min ramp) to produce phase-pure wurtzite ZnO powder (XRD-confirmed, JCPDS 01-079-0206). Screen printing paste was formulated with calcined powder ($D_{50} \approx 150$ nm) in ethyl cellulose/α-terpineol vehicle. Structural characterization via XRD (Cu-Kα: $\lambda = 1.5406$ Å, 40 kV/15 mA) revealed intense (100), (002), and (101) reflections consistent with hexagonal wurtzite symmetry ($P6_3mc$ space group). Crystallite size (D) and microstrain (ε) were quantified using Scherrer's equation ($D = K\lambda/\beta\cos\theta$) and Williamson-Hall analysis ($\beta\cos\theta = K\lambda/D + 4\varepsilon\sin\theta$). Scherrer-derived crystallite sizes exceeded W-H values (Table 1), indicating residual strain contributions. Microstrain elevation correlated with increased dislocation density and vacancy defects. This work establishes correlations between synthesis-induced defects, microstrain, and functional properties in printed ZnO films.*

Keywords: Thick film; Zinc Oxide; Sceen Printing; XRD; W-H Plot

I. INTRODUCTION

Thick-film technology represents a unique convergence of ancient fabrication arts and modern materials science. As a cornerstone of microelectronics and optoelectronics, thick-film components serve as critical technological drivers underpinning significant sectors of the global economy, evidenced by their pervasive use in communications infrastructure, information processing systems, data storage solutions, and display technologies [1]. Advancements in deposition methodologies have further catalyzed the expansion of thick-film applications into diverse domains, including functional coatings, biotechnology, and energy generation/conversion systems [2]. Fundamentally, the development and optimization of thick-film applications are deeply rooted in materials science and engineering principles. The historical utilization of thick-film techniques dates back to antiquity, notably during early metallurgical periods. Processing materials into thick-film configurations facilitates their integration into a wide array of device architectures [3]. Critically, the physical, chemical, and functional properties of materials often exhibit significant deviations when configured as thick films compared to their bulk counterparts [4]. Consequently, many functional materials are preferentially applied in thick-film form to exploit specific desirable characteristics such as tailored electrical conductivity, magnetic permeability, optical properties (e.g., transmittance, reflectance), or enhanced wear resistance [5]. This versatility has spurred growing scientific and technological interest in thick films, leading to their deployment across numerous fields. Key applications encompass photovoltaics, microelectronic circuits, thermoelectric devices, superconductors, information storage media, solid oxide fuel cells (SOFCs), biocompatible coatings, solar cells, and light-emitting diodes (LEDs) [6]. Recently, nanocrystalline thick films have attracted significant research attention due to their advantageous properties relative to conventional coarse-grained materials. These include a high specific surface area, enhanced atomic diffusivity, reduced density, elevated electrical resistivity, increased mechanical strength, and modified magnetic properties (e.g., superparamagnetism) [7, 8]. The requisite properties of thick films are intrinsically linked to their application. Critical performance metrics often include optical characteristics

(reflectance/transmittance spectra), mechanical hardness, tribological wear resistance, and the degree of crystallinity (ranging from polycrystalline to single-crystal-like) [5, 9, 10]. These properties can be precisely engineered through careful selection and optimization of the deposition technique. Thick-film deposition methodologies are broadly classified as physical vapor deposition (PVD) or chemical deposition based on the fundamental processes involved [11]. PVD techniques, such as thermal evaporation and magnetron sputtering, involve the physical transfer of material in a vacuum environment [12]. Conversely, chemical deposition techniques facilitate film growth through chemical reactions, occurring either from the gas phase (e.g., Chemical Vapor Deposition - CVD) or the liquid phase [13]. Liquid-phase chemical synthesis techniques include electrodeposition, chemical bath deposition (CBD) [14], successive ionic layer adsorption and reaction (SILAR) [15], and spray pyrolysis [16]. These chemical routes offer distinct advantages, including precise stoichiometric control, cost-effectiveness, scalability, and lower processing temperatures conducive to flexible substrates or temperature-sensitive materials [17-20]. Nanotechnology is widely employed for the detection and treatment of diseases [21], improvement of agricultural crops [22], industry, and academic fields [23]. Due to their distinctive qualities, such as aspect ratio, thick film play a significant role in nanotechnology and are more beneficial in many applications than conventional materials [24]. Among the different categories of thick film, viz. metal, polymer, ceramic, carbon, lipid, and metal oxides etc.; the ZnO metal oxide semiconductor nanoparticle has distinct properties such as a wide band gap of ~ 3.37 eV, the high binding energy of excitation ~60 meV, and high bond strength, photo luminance, electrochemical properties, electrical properties [25-27]. These fundamental properties has increased the ZnO participation in several applications like drug delivery [28], anticancer [29], gas sensors [30], cosmetics [31], solar cells [32] etc. In certain applications, the combination of two metal oxide semiconductors has a unique function. ZnO is regarded as the most significant of the several varieties of two-metal oxides and has attracted the attention of numerous researchers due to its superior performance to other semiconductors in catalysts, solar cells, sensors, and optoelectronic devices [33, 34]. ZnO, a broad bandgap semiconductor with a hexagonal wurtzite crystal structure, has emerged as a key material for many technological breakthroughs. Its abundance, non-toxicity, and superior physical and chemical qualities make it a less expensive and more ecologically friendly alternative to conventional semiconductors. ZnO has exceptional features, such as high transparency, electrical conductivity, piezoelectric behavior, and strong photocatalytic activity. This study presents a complete review of ZnO, looking at its fundamental properties, production techniques, and many uses.

Recent advancements in ZnO

Research endeavors are consistently focused on augmenting the capabilities of zinc oxide. Techniques for surface modification, such as adding functional groups or doping with additional elements, allow the material's bandgap, electrical conductivity, and surface reactivity to be customized for particular uses. Significant advancements have also been achieved in the creation of ZnO nanostructures in a variety of morphologies, including nanowires, nanotubes, and nanosheets [35, 36]. These nanostructures' enhanced surface area and effective light interaction provide them better qualities than thick film. ZnO is a good choice for transparent conducting oxide (TCO) electrodes in solar cells and light-emitting diodes (LEDs) due to its transparency and conductivity [36, 37]. Surface acoustic wave (SAW) devices and transducers both use its piezoelectric qualities [38]. Due to the superior photocatalytic activity of zinc oxide, it may break down organic contaminants and produce hydrogen fuel by splitting water when exposed to UV light. Zinc Oxide (ZnO) has potential in dye-sensitized solar cells (DSSCs) and lithium-ion batteries because of its capacity to absorb light and store lithium [39, 40]. ZnO is a promising option for gas sensors and biosensors due to its great sensitivity to a wide range of gases and biomolecules. The antibacterial and biocompatible characteristics of ZnO make it a promising material for use in bone implants [41], wound healing dressing [42], and drug delivery systems [43]. ZnO still has a lot of promise, and future studies can look into Doping and composite formation [44, 45].

II. EXPERIMENTAL

2.1 Materials

High-purity anhydrous zinc chloride ($ZnCl_2$, 99.99%, Sigma-Aldrich) and sodium hydroxide pellets (NaOH, ≥97%, Merck) were dissolved in deionized water (18.2 MΩ·cm, Milli-Q) to formulate precursor solutions. For screen printing,

IJETIR
ISSN (Online) 2583-0554
International Journal of Emerging Technologies and Innovative Research (IJETIR)
Volume 3, Issue 3, March 2023
Impact Factor: 5.731

calcined ZnO powder was blended with an organic vehicle comprising ethyl cellulose (Sigma-Aldrich 200646) and α-terpineol (Alfa Aesar A16270) at a 1:9 (w/w) ratio, supplemented with oleic acid dispersant (90%, Fisher Scientific). glass substrates (25 × 25 × 1 mm, Ted Pella) were cleaned using HPLC-grade acetone (Sigma-Aldrich) and isopropanol (≥99.5%, Honeywell). Post-printing sintering utilized DuPont™ 7713 silver paste for electrical contacts. muffle furnace, screen printer (325-mesh screen).

2.2 Fabrication of ZnO thick film

A 0.5 M zinc chloride ($ZnCl_2$) precursor solution was prepared by dissolving stoichiometric quantities of $ZnCl_2$ in 100 mL of deionized water under continuous magnetic stirring (500 rpm) until complete dissolution. Concurrently, a 1.0 M sodium hydroxide (NaOH) solution was formulated by dissolving NaOH pellets in 100 mL of deionized water, followed by 15 minutes of magnetic agitation to ensure homogeneity. The co-precipitation reaction was initiated by dropwise addition (2 mL/min) of the NaOH solution into the $ZnCl_2$ precursor under vigorous stirring (800 rpm), yielding a milky-white zinc hydroxide $[Zn(OH)_4]^{2-}$ colloidal suspension. The precipitate was isolated via vacuum filtration using a 0.2 µm cellulose membrane and purified through five washing cycles with deionized water to eliminate chloride ions and residual sodium. The filtered cake underwent ambient drying (25°C, 24 h) followed by mechanical comminution in an agate mortar to achieve a uniform particle size distribution (D_{50} ≈ 150 nm). Calcination was performed in a muffle furnace at 400°C for 2 h (ramp rate: 5°C/min) under atmospheric conditions, converting intermediates to crystalline ZnO powder (wurtzite phase, confirmed by XRD).

Screen Printing Process:

- **Paste Formulation:** The calcined ZnO powder was blended with an organic vehicle (ethyl cellulose: α-terpineol, 1:9 wt%) at 30 wt% solids loading. The mixture underwent triple-roll milling (gap: 5 µm) to achieve rheological stability (viscosity: 12–15 kcP at 25°C).
- **Substrate Preparation:** Glass slides (25 × 25 mm) were ultrasonically cleaned in acetone/IPA and oxygen-plasma treated (100 W, 5 min) to enhance adhesion.
- **Printing:** The ZnO paste was deposited through a 325-mesh stainless-steel screen (emulsion thickness: 20 µm) using a semi-automatic printer (squeegee pressure: 2.5 bar, speed: 10 mm/s).
- **Drying & Sintering:** Printed films were leveled (10 min), dried at 120°C (15 min), and sintered at 550°C for 1 h (ramp: 2°C/min) to burn out organics and ensure particle consolidation.

Post-Fabrication Characterization:

Film thickness (15.3 ± 0.8 µm) was verified by profilometry. Microstructural analysis revealed dense polycrystalline morphology with 85–92% theoretical density and average grain size of 0.7–1.2 µm. The thermal decomposition process during calcination promotes the formation of metal oxide nanostructures through the following chemical transformation pathway:

$$ZnCl_{2(aq)} + 2Na(OH)_{(aq)} \rightarrow Zn(OH)_{2(S)} \downarrow + 2NaCl_{(aq)} \quad (1)$$

$$Zn^{2+}_{(aq)} + 2Cl^{1-}_{(aq)} + 2Na^{1+}_{(aq)} + 2(OH)^{1-}_{(aq)} \rightarrow Zn(OH)_{2(S)} \downarrow + 2Na^{1+}_{(aq)} + 2Cl^{1-}_{(aq)} \quad (2)$$

The final equation is:

$$Zn^{2+}_{(aq)} + 2(OH)^{1-}_{(aq)} \rightarrow Zn(OH)_{2(S)} \downarrow \quad (3)$$

And after dissociation reaction becomes:

$$Zn(OH)_{2(S)} \downarrow \xrightarrow{\Delta} ZnO_{(S)} \downarrow + H_2O_{(g)} \quad (4)$$

IJETIR
ISSN (Online) 2583-0554
International Journal of Emerging Technologies and Innovative Research (IJETIR)
Volume 3, Issue 3, March 2023
Impact Factor: 5.731

2.4 Characterization of Samples

The X-ray diffraction (XRD) pattern of the ZnO thick film (NPs) was acquired using a Rigaku MiniFlex diffractometer equipped with a Cu Kα radiation source (λ = 1.54060 Å). Measurements were performed over a 2θ range from -3° to 145° at a scanning rate of 2° per minute, with instrument settings of 40 kV, 15 mA, and a maximum power of 600 W.

III. RESULT AND DISCUSSION

3.1 Crystal structure of ZnO

Zinc oxide (ZnO) adopts the wurtzite structure, a hexagonal Bravais lattice characterized by tetrahedral coordination of Zn^{2+} cations by O^{2-} anions. This specific atomic arrangement generates intrinsic spontaneous polarization along the crystallographic c-axis, a key factor underlying ZnO's pronounced piezoelectric properties. ZnO possesses a wide direct bandgap semiconductor, approximately 3.3 eV at room temperature. This substantial bandgap energy facilitates efficient ultraviolet (UV) photon absorption, rendering ZnO highly suitable for photocatalytic applications. Furthermore, ZnO typically exhibits intrinsic n-type semiconducting behavior, characterized by facile electron donation, high carrier mobility, and consequently, significant electrical conductivity. The fundamental building block of the wurtzite lattice is a hexagonal unit cell. It comprises two interpenetrating hexagonal close-packed (hcp) sublattices offset along the c-axis: one sublattice consists of oxygen anions and the other of zinc cations. Within this structure, each anion is tetrahedrally coordinated by four cations, and conversely, each cation is tetrahedrally coordinated by four anions. The oxygen anions form close-packed layers in the basal plane with an ABAB... stacking sequence, where each successive layer is translated relative to the preceding one. Zinc cations occupy precisely half of the available tetrahedral interstices within this anion framework. Due to the ABAB stacking, these cations reside in alternating sets of tetrahedral voids (denoted A and B sites) between successive anion layers. The wurtzite structure is defined by three principal crystallographic axes: two equivalent basal plane axes (a_1 and a_2) intersecting at 120°, and the polar c-axis perpendicular to the basal plane. The lattice parameters typically exhibit a c/a axial ratio less than the ideal value for hexagonal close-packing. The non-centrosymmetric wurtzite structure belongs to the $P6_3mc$ space group, reflecting the absence of inversion symmetry inherent to this polar crystal structure.

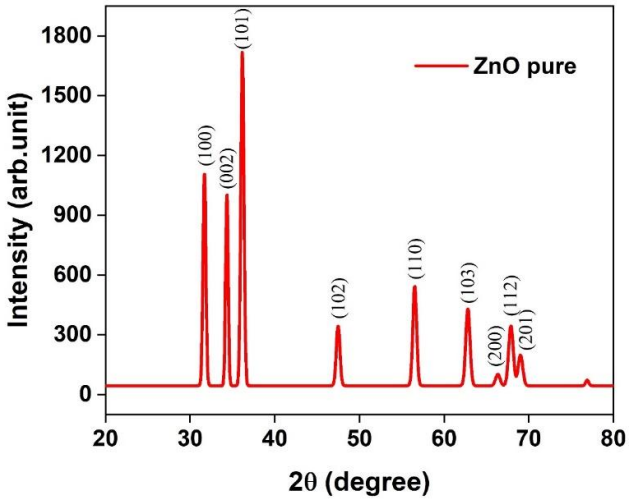

Figure 2. X-ray diffraction pattern of screen printed ZnO thick film

The XRD identifies the Bragg's reflections at 2θ degree to the Miller indices in the Cartesian coordinate system as (100), (002), (101), (102), (110), (103), (200), (112), and (201) hkl planes respectively [46]. The X-ray reflections matches with JCPDS card No.01-079-0206 of ZnO. According to D.M. Fernandes et al. the emergence of two phases for ZnO verifies the effective synthesis of Thick film [47]. The calculation for the interplanar spacing (d_{hkl}) was done by Bragg's Law [48] eq. (12)

IJETIR
ISSN (Online) 2583-0554
International Journal of Emerging Technologies and Innovative Research (IJETIR)
Volume 3, Issue 3, March 2023
Impact Factor: 5.731

$$n\lambda = 2d_{hkl} \sin\theta \quad (12)$$

Where n =1 is the order of diffraction, λ= 0.15406 nm; is the wavelength of the X-ray, (d_{hkl}) is the interplanar spacing and the θ is the angle between the incident ray to the crystal planes. The dislocation density δ is calculated by eq. (13) [49];

$$\delta = \frac{1}{D^2} \quad (13)$$

The crystallite size is denoted by D. The calculated interplanar spacing (d_{hkl}) and dislocation density (δ) are presented in **Table 1.**

Table 1. Lattice constant (a) Å, the crystallite size (D), Crystallinity (%), Dislocation density, Lattice strain, Microstrain, for the screen printed ZnO thick film

Lattice Constant Å		**D (Sherrer)**	**D (W-H)**	**Crystallinity**	**dislocation density**	**lattice strain**	**Macrostrain**
a	**c**	**(nm)**	**(nm)**	**(%)**	**δ*10^3 (nm^-2)**	**ε*10^-3**	**10^-4**
2.5	6.894	25	49	**71**	6.08	0.54	-183.3

Lattice parameters (a, b, c) for the hexagonal wurtzite phase, These values align with the reference crystallographic standards for ZnO thick film from the Joint Committee on Powder Diffraction Standards (JCPDS) database (Card No. 36-1451), which catalogs structural parameters for zinc oxide. Specifically, The lattice constants (a) of the hexagonal structure was determined by the eq. (14) [50]:

$$\frac{1}{d^2_{hkl}} = \frac{4}{3}\left[\frac{h^2+hk+k^2}{a^2}\right] + \frac{l^2}{c^2} \quad (14)$$

Where, (d_{hkl}) is interplanar spacing, (hkl) is Miller indices, a and c are the lattice constants. The lattice constants of the monoclinic structure have been determined using the eq. (15) at the ZnO NCP,;

$$\frac{1}{d^2_{hkl}} = \left[\frac{h^2}{a^2} + \frac{k^2 sin^2\beta}{b^2} + \frac{l^2}{c^2} - \frac{2hlcos\beta}{ac}\right] * csc^2\beta \quad (15)$$

Where, ($csc^2\beta$) is ($\frac{1}{sin^2\beta}$), β = 99.75°, and a ≠ b ≠ c are the lattice constants belongs to the monoclinic structure as shown in a **Table.** The crystal structure features a trigonal prismatic coordination environment where octahedrally coordinated Zn^{2+} ions (ionic radius = 0.82 Å) are each surrounded by six O^{2-} anions. A relative displacement of adjacent ZnO layers along the crystallographic c-axis generates the monoclinic unit cell. These displaced layers are subsequently stabilized by weak interlayer van der Waals forces, resulting in a robust structural framework. The significant difference between the ionic radii of Zn^{2+} (0.82 Å) and O^{2-} (~1.40 Å) is consistent with the observed coordination geometry and structural stability. The Debye-Scherrer equation, which is given by eq. (16):

$$D = \frac{K*\lambda}{\beta*cos\theta} \quad (16)$$

where λ=0.15406 nm (Cu Kα radiation wavelength), K=0.9 (Scherrer's constant), β denotes the full width at half maximum (FWHM) of the diffraction peak, and θ is the Bragg angle. Crystallite dimensions for all samples were evaluated via two methodologies: (i) analysis at the highest-intensity peak and (ii) averaging across multiple peaks as tabulated in **Table 1.** Complementarily, the Williamson-Hall (W-H) method employing the uniform deformation model

IJETIR
ISSN (Online) 2583-0554
International Journal of Emerging Technologies and Innovative Research (IJETIR)
Volume 3, Issue 3, March 2023
Impact Factor: 5.731

(UDM) was applied to deconvolute size and strain contributions to peak broadening. The W-H technique correlates βcosθ with 4sinθ to simultaneously compute crystallite size and lattice microstrain (ε), expressed as [51]:

$$Total\ broadening = crystallite\ size\ broadening + strain\ broadening$$

$$\beta_T = \beta_D + \beta_\varepsilon$$

$$\beta_T = \frac{k\lambda}{Dcos\theta} + 4\varepsilon tan\theta$$

$$where: D = \frac{k\lambda}{\beta_D cos\theta}, \varepsilon = \frac{\beta_\varepsilon}{4tan\theta}, tan\theta = \frac{sin\theta}{cos\theta}$$

$$\beta_T = \frac{k\lambda}{Dcos\theta} + 4\varepsilon\frac{sin\theta}{cos\theta}$$

$$\beta_T cos\theta = \frac{k\lambda}{D} + 4\varepsilon sin\theta$$

or

$$\beta_T cos\theta = \varepsilon(4sin\theta) + \frac{k\lambda}{D} \quad (17)$$

Equation (17) represents the Williamson-Hall (W-H) method, where the crystallite size D is derived from the y-axis intercept ($\frac{k\lambda}{D}$).

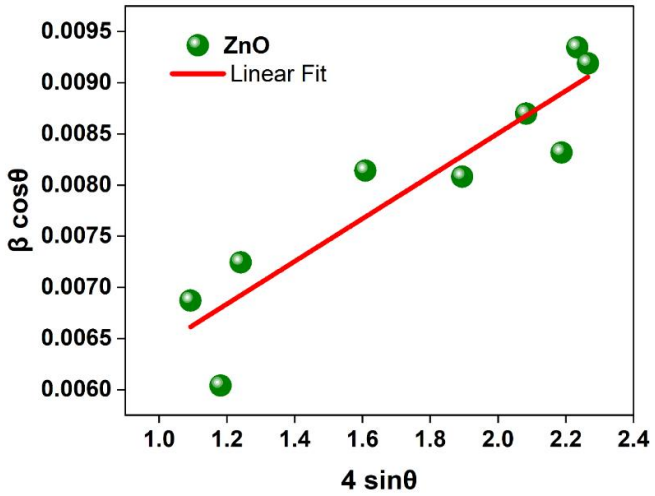

Figure 5. Williamson-Hall plots of screen printed ZnO thick film

In the associated plot (**Figure 3**), the x-axis corresponds to 4sinθ, while the y-axis denotes βTcosθ. The slope εε quantifies the induced microstrain. Analysis reveals that crystallite sizes calculated via the Scherrer equation consistently exceed those determined by W-H analysis (**Table 1**). Furthermore, the microstrain ε increases proportionally with dislocation density, attributed to lattice distortions and vacancy defects. The constrained nanoparticle dimensions are consistent with the Zener pinning effect [52]. wherein zinc ions impede grain growth by stabilizing grain boundaries. This phenomenon occurs when nanoparticle size approaches the material's lattice

parameter, enhancing crystalline stability and promoting a narrow size distribution. Consequently, these nanocrystals exhibit improved functional properties, including enhanced magnetic behavior and superior chemical stability, while reduced dimensions facilitate practical application integration. Morphological analysis (**Figure 2**) indicates that XRD data further demonstrate reduced crystallinity in ZnO thick film. The crystallinity was calculated by using eq. 18:

$$CI(\%) = \frac{area\ of\ all\ crystalline\ peaks}{area\ of\ all\ peaks[crystallite + amorphous\ ]} \qquad (18)$$

IV. CONCLUSIONS

Zinc oxide is a substance that has remarkable properties and is both versatile and promising. Its wide range of applications in many industries demonstrate how much technical progress it can make. ZnO will probably have more applications in the future in technologies that focus on surface modification, nanostructuring, and composite synthesis with other materials. In this work was the fabrication of ZnO Thick film by using the chemical co-precipitation method. We reached a successful thick film. Where the samples have been subjected to different analyses such as XRD. Miller indices in the Cartesian coordinate system as (100), (002), (101), (102), (110), (103), (200), (112), and (201) hkl planes respectively. In XRD analysis has appeared peaks for two structures that were related to ZnO with lesser crystal size. All those outcomes have confirmed that the fabrication of ZnO Thick film has been successful.

REFERENCES

[1] K. Pitt, Handbook of thick film technology, Soldering & Surface Mount Technology, 18 (2006) 45-45.
[2] J. Larry, R. Rosenberg, R. Uhler, Thick-film technology: an introduction to the materials, IEEE transactions on components, hybrids, and manufacturing technology, 3 (1980) 211-225.
[3] S. Rane, T. Seth, G. Phatak, D. Amalnerkar, B. Das, Influence of surfactants treatment on silver powder and its thick films, Materials Letters, 57 (2003) 3096-3100.
[4] M. Sayer, K. Sreenivas, Ceramic thin films: fabrication and applications, Science, 247 (1990) 1056-1060.
[5] N. White, Thick films, Springer Handbook of Electronic and Photonic Materials, DOI (2017) 1-1.
[6] N.Q. Minh, T.R. Armstrong, J.R. Esopa, J.V. Guiheen, C.R. Home, J.J. Van Ackeren, Tape-Calendered Monolithic and Flat Plate Solid Oxide Fuel Cells, ECS Proceedings Volumes, 1993 (1993) 801.
[7] H. Hahn, Unique features and properties of nanostructured materials, Nanomaterials by Severe Plastic Deformation, DOI (2004) 2-17.
[8] H. Gleiter, Nanostructured materials: basic concepts and microstructure, Acta materialia, 48 (2000) 1-29.
[9] J.A. Thornton, High rate thick film growth, Annual review of materials science, 7 (1977) 239-260.
[10] O.S. Heavens, Optical properties of thin films, Reports on Progress in Physics, 23 (1960) 1.
[11] P. Panjan, A. Drnovšek, P. Gselman, M. Čekada, M. Panjan, Review of growth defects in thin films prepared by PVD techniques, Coatings, 10 (2020) 447.
[12] B. Tlili, C. Nouveau, M.J. Walock, M. Nasri, T. Ghrib, Effect of layer thickness on thermal properties of multilayer thin films produced by PVD, Vacuum, 86 (2012) 1048-1056.
[13] A. Obraztsov, E. Obraztsova, A. Tyurnina, A. Zolotukhin, Chemical vapor deposition of thin graphite films of nanometer thickness, Carbon, 45 (2007) 2017-2021.
[14] C. Pérez-García, R. Ramírez-Bon, Y. Vorobiev, PbS thin films growth with CBD and PCBD techniques: a comparative study, Chalcogenide Letters, 12 (2015) 579-588.
[15] S.P. Ratnayake, J. Ren, E. Colusso, M. Guglielmi, A. Martucci, E. Della Gaspera, SILAR deposition of metal oxide nanostructured films, Small, 17 (2021) 2101666.
[16] D. Perednis, L.J. Gauckler, Thin film deposition using spray pyrolysis, Journal of electroceramics, 14 (2005) 103-111.
[17] F. Toma, S. Rahman, K.M. Hussain, S. Ahmed, Thin film deposition techniques: a comprehensive review, J Mod Nanotechnol, 4 (2024).

[18] K.P. Musselman, C.F. Uzoma, M.S. Miller, Nanomanufacturing: high-throughput, cost-effective deposition of atomic scale thin films via atmospheric pressure spatial atomic layer deposition, Chemistry of Materials, 28 (2016) 8443-8452.
[19] H. Kozuka, S. Takenaka, H. Tokita, T. Hirano, Y. Higashi, T. Hamatani, Stress and cracks in gel-derived ceramic coatings and thick film formation, Journal of Sol-Gel Science and Technology, 26 (2003) 681-686.
[20] M. Koch, N. Harris, A.G. Evans, N.M. White, A. Brunnschweiler, A novel micromachined pump based on thick-film piezoelectric actuation, Sensors and Actuators A: Physical, 70 (1998) 98-103.
[21] B. Purnama, A.T. Wijayanta, Effect of calcination temperature on structural and magnetic properties in cobalt ferrite nano particles, Journal of King Saud University-Science, 31 (2019) 956-960.
[22] S. Altabbaa, N.A. Mann, N. Chauhan, K. Utkarsh, N. Thakur, G.A.-E. Mahmoud, Era connecting nanotechnology with agricultural sustainability: issues and challenges, Nanotechnology for Environmental Engineering, 8 (2023) 481-498.
[23] I. Kang, J. Yang, W. Lee, E.-Y. Seo, D.H. Lee, Delineating development trends of nanotechnology in the semiconductor industry: Focusing on the relationship between science and technology by employing structural topic model, Technology in Society, 74 (2023) 102326.
[24] S. Shah, P. Famta, D. Bagasariya, K. Charankumar, E. Amulya, D.K. Khatri, R.S. Raghuvanshi, S.B. Singh, S. Srivastava, Nanotechnology based drug delivery systems: Does shape really matter?, International Journal of Pharmaceutics, DOI (2022) 122101.
[25] P. Halappa, H.M. Rajashekar, C. Shivakumara, Synthesis and structural characterization of orange red light emitting Sm3+ activated BiOCl phosphor for WLEDs applications, Journal of Alloys and Compounds, 785 (2019) 169-177.
[26] S. Pramanik, S. Mukherjee, S. Dey, S. Mukherjee, S. Das, T. Ghosh, P. Ghosh, R. Nath, P.K. Kuiri, Cooperative effects of zinc interstitials and oxygen vacancies on violet-blue photoluminescence of ZnO nanoparticles: UV radiation induced enhanced latent fingerprint detection, Journal of Luminescence, 251 (2022) 119156.
[27] D. Han, X.-B. Li, D. Wang, N.-K. Chen, X.-W. Fan, Doping in the two-dimensional limit: p/n-type defects in monolayer ZnO, Physical Review B, 105 (2022) 024104.
[28] A. Sathiyaseelan, K. Saravanakumar, X. Zhang, K.V. Naveen, M.-H. Wang, Ampicillin-resistant bacterial pathogens targeted chitosan nano-drug delivery system (CS-AMP-P-ZnO) for combinational antibacterial treatment, International Journal of Biological Macromolecules, 237 (2023) 124129.
[29] N. Elavarasan, S. Vignesh, M. Srinivasan, G. Venkatesh, G. Palanisamy, P. Ramasamy, B. Palanivel, A.M. Al-Enizi, M. Ubaidullah, V.R.M. Reddy, Synergistic S-Scheme mechanism insights of g-C3N4 and rGO combined ZnO-Ag heterostructure nanocomposite for efficient photocatalytic and anticancer activities, Journal of Alloys and Compounds, 906 (2022) 164255.
[30] M.A. Franco, P.P. Conti, R.S. Andre, D.S. Correa, A review on chemiresistive ZnO gas sensors, Sensors and Actuators Reports, 4 (2022) 100100.
[31] R. Chauhan, A. Kumar, R. Tripathi, A. Kumar, Advancing of zinc oxide nanoparticles for cosmetic applications, Handbook of consumer Nanoproducts, Springer2022, pp. 1-16.
[32] Y. Wang, Z. Zheng, J. Wang, X. Liu, J. Ren, C. An, S. Zhang, J. Hou, New Method for Preparing ZnO Layer for Efficient and Stable Organic Solar Cells, Advanced Materials, 35 (2023) 2208305.
[33] A. Chatterjee, A. Ravindra, G.K. Kumar, C. Rajesh, Improvement in the light conversion efficiency of silicon solar cell by spin coating of CuO, ZnO nanoparticles and CuO/ZnO mixed metal nanocomposite material, Journal of the Indian Chemical Society, 99 (2022) 100653.
[34] H. Safdar, R. Aydın, B. Şahin, Syntheses, structural evolution, electrical and optoelectronic characterization of ZnO/CuO composite films doped with transition metal Mn2+ ions, Ceramics International, 48 (2022) 26678-26688.
[35] S.G. Kumar, K.K. Rao, Zinc oxide based photocatalysis: tailoring surface-bulk structure and related interfacial charge carrier dynamics for better environmental applications, Rsc Advances, 5 (2015) 3306-3351.
[36] Z. Luo, P. Rong, Z. Yang, J. Zhang, X. Zou, Q. Yu, Preparation and application of co-doped zinc oxide: a review, Molecules, 29 (2024) 3373.

[37] G.T. Chavan, Y. Kim, M.Q. Khokhar, S.Q. Hussain, E.-C. Cho, J. Yi, Z. Ahmad, P. Rosaiah, C.-W. Jeon, A brief review of transparent conducting oxides (TCO): the influence of different deposition techniques on the efficiency of solar cells, Nanomaterials, 13 (2023) 1226.
[38] M.R. Zakaria, S. Johari, M.H. Ismail, U. Hashim, Characterization of zinc oxide (ZnO) piezoelectric properties for surface acoustic wave (SAW) device, EPJ Web of conferences, EDP Sciences, 2017, pp. 01055.
[39] Q. Zhang, C.S. Dandeneau, S. Candelaria, D. Liu, B.B. Garcia, X. Zhou, Y.-H. Jeong, G. Cao, Effects of lithium ions on dye-sensitized ZnO aggregate solar cells, Chemistry of Materials, 22 (2010) 2427-2433.
[40] M. Saeed, H.M. Marwani, U. Shahzad, A.M. Asiri, M.M. Rahman, Recent advances, challenges, and future perspectives of ZnO nanostructure materials towards energy applications, The Chemical Record, 24 (2024) e202300106.
[41] K.E. Mokobia, I.H. Ifijen, E.U. Ikhuoria, ZnO-NPs-coated implants with osteogenic properties for enhanced osseointegration, TMS Annual Meeting & Exhibition, Springer, 2023, pp. 288-300.
[42] Z. Lu, J. Gao, Q. He, J. Wu, D. Liang, H. Yang, R. Chen, Enhanced antibacterial and wound healing activities of microporous chitosan-Ag/ZnO composite dressing, Carbohydrate polymers, 156 (2017) 460-469.
[43] U. Chawla, D. Dahiya, Y. Kumar, A. Bala, M. Genwa, N. Agasti, S. Tandon, S.P. Singh, P. Meena, A review on ZnO-based targeted Drug Delivery System, Letters in Drug Design & Discovery, 21 (2024) 397-420.
[44] H.B. Dias, M.I.B. Bernardi, V.S. Marangoni, A.C. de Abreu Bernardi, A.N. de Souza Rastelli, A.C. Hernandes, Synthesis, characterization and application of Ag doped ZnO nanoparticles in a composite resin, Materials Science and Engineering: C, 96 (2019) 391-401.
[45] J. Morales-Mendoza, G. Herrera-Pérez, L. Fuentes-Cobas, L. Hermida-Montero, N. Pariona, F. Paraguay-Delgado, Synthesis, structural and optical properties of Cu doped ZnO and CuO–ZnO composite nanoparticles, Nano-Structures & Nano-Objects, 34 (2023) 100967.
[46] S. Vijayakumar, B. Vaseeharan, B. Malaikozhundan, M. Divya, M. Abhinaya, N. Gobi, A. Bhattacharyya, N. Balashanmugam, D. Surmistha, K. Murugan, Ecotoxicity of Musa paradisiaca leaf extract-coated ZnO nanoparticles to the freshwater microcrustacean Ceriodaphnia cornuta, Limnologica, 67 (2017) 1-6.
[47] D. Fernandes, R. Silva, A.W. Hechenleitner, E. Radovanovic, M.C. Melo, E.G. Pineda, Synthesis and characterization of ZnO, CuO and a mixed Zn and Cu oxide, Materials chemistry and physics, 115 (2009) 110-115.
[48] S.B. Gopale, M.V. Khedkar, S.A. Jadhav, A.V. Raut, S.S. Karad, G.D. Kulkarni, K. Jadhav, Influence of Al3+-Gd3+ co-substitution on the structural, morphological, magnetic and optical properties of nickel ferrite nanoparticles, Journal of Materials Science: Materials in Electronics, 33 (2022) 26544-26563.
[49] E.A. Volnistem, R.C. Oliveira, G.H. Perin, G.S. Dias, M.A. de Melo, L.F. Cótica, I.A. Santos, S. Süllow, D. Baabe, F.J. Litterst, Controlled dislocation density as enhancer of the magnetic response in multiferroic oxide nanoparticles, Applied Materials Today, 29 (2022) 101680.
[50] P. Norouzzadeh, K. Mabhouti, M. Golzan, R. Naderali, Investigation of structural, morphological and optical characteristics of Mn substituted Al-doped ZnO NPs: a Urbach energy and Kramers-Kronig study, Optik, 204 (2020) 164227.
[51] A.G. Patil, A.P. Keche, S. Rajmane, A.V. Raut, W–H plot and electron spin resonance spectroscopy of magnetic CoFNPs induced up to 100 kGy Co60 γ-rays, Radiation Effects and Defects in Solids, 177 (2022) 847-868.
[52] G. Hu, L. Zeng, H. Du, Q. Wang, Z. Fan, X. Liu, Combined effects of solute drag and Zener pinning on grain growth of a NiCoCr medium-entropy alloy, Intermetallics, 136 (2021) 107271.